TECHNICAL ARTICLE

On 3D-Printed Acrylonitrile Butadiene Styrene-Based Sensors: Rheological, Mechanical, Morphological, Radio Frequency, and 4D Capabilities

Chahat Jain, Balwinder S. Dhaliwal, and Rupinder Singh

Acrylonitrile butadiene styrene (ABS) one of the recyclable thermoplastics having insulating properties is being widely used as a 3D-printed substrate for Bluetooth sensing devices. But hitherto little has been reported on the 4D capabilities of 3D-printed recyclable ABS substrate-based sensors. This study reports the rheological (melt flow), mechanical (tensile), morphological (surface hardness, roughness (Ra), porosity, etc.), 3D printability, and radio frequency (RF) characteristics of primary recycled ABS substrate. Further, the 3D-printed ABS substrate samples were exposed to two different stimuli (chemical and thermal) for 10 cycles/stages to ascertain the effect on RF characteristics for ensuring 4D capabilities. The 3D-printed Bluetooth sensor has been designed for 2.45 GHz. The simulated results of the 3D-printed prototypes were verified experimentally using a vector network analyzer (VNA), which shows the appreciable response with a minimal frequency shift, thus ensuring the applicability of such sensors for Bluetooth applications. The percentage variation in the dielectric constant has been recorded to a maximum of 8% (in stage 9) and a minimum of 2% (in stage 6). Also, the dissipation factor of the substrate has been recorded to remain constant (~0.0045) indicating a factor of repeatability and hence the usability of such materials for 4D printing applications. Morphological analysis on scanning electron microscopy (SEM) reveals that the Ra of the 3D-printed ABS substrate was significantly improved (50-19 nm), hence ensuring better performance of the fabricated sensors.

1. Introduction

During the past few decades, planar antennas/sensors have gathered a lot of attention due to their low profile and conformability (Ref 1, 2). As electronics technology is evolving at a rapid pace, the demands for compact and lightweight materials have increased than ever before (Ref 3). Organic substrates such as polymers and papers offer more eco-friendly options for the fabrication of compact devices than substrates like FR-4, silicon, etc. (Ref 3, 4). Moreover, they provide a great advantage of flexibility and wearability. It has been reported that by using the technology of 3D printing, one can design any complex structure by the successive layer by layer construction, thus circumventing the requirement for machining. Due to less wastage of material, more cost-efficient prototypes can be rapidly manufactured (Ref 5, 6).

ABS being a non-toxic material has been widely opted to develop antenna prototypes (Ref 7-10). Also, due to its recyclability and insulating nature, it can perfectly serve as a substrate to build different kinds of flexible and wearable antennas/sensors. In one of the recent studies, conducting ABS was investigated for the fabrication of a 3D-printed bowtie flexible antenna which achieves a wide bandwidth of 24.18% and also shows good mechanical robustness, thus proving its functionality for the fabrication of 3D-printed electromagnetic structures (Ref 8). Apart from ABS, other organic 3D-printed antennas make use of paper-based substrates (Ref 9, 10). In the recent past, with inkjet printing, a Z-shaped antenna has been developed using silver nanoparticle ink which is comparatively cheaper than the corresponding counterparts (Ref 11). A U slot monopole antenna which was inkjet-printed for applications covering bands like GPS, WiMAX, Hiper LAN/2, and WLAN has been reported to achieve a compact size, hence leaving enough space for the other driving electronics to be fabricated on the paper substrate (Ref 10). Also, substrates such as Kapton polyimide films have been investigated for their flexibility analysis (Ref 11). It has been observed that such substrates serve appreciable functionality over several frequency bands under various deformity conditions. Besides the availability of different varieties of substrates, researchers in recent years have opted for tailor printed substrates where the usage of heterogeneous substrates has guaranteed the applicability of antennas to biocompatible and flexible applications (Ref 12-14). How-

Chahat Jain, Department of Electronics Engineering, I.K. Gujral Punjab Technical University, Jalandhar, India; and Department of Electronics and Communication Engineering, Guru Nanak Dev Engineering College, Ludhiana, India; Balwinder S. Dhaliwal, Department of Electronics and Communication Engineering, National Institute of Technical Teachers Training and Research, Chandigarh, India; and Rupinder Singh, Department of Mechanical Engineering, National Institute of Technical Teachers Training and Research, Chandigarh, India. Contact e-mail: rupindersingh@nitttrchd.ac.in.

ever, the characterization of such substrates is a big challenge as far as the antenna functionality is concerned. For that, different characterization techniques have been investigated by the researchers (Ref 1, 2, 12, 13, 15, 16). Researchers have used different 3D printing techniques such as laser sintering, inkjet printing, vat photo-polymerization, and fused deposition modeling (FDM). (Ref 14-16).

The technique of 4D printing may be extensively used for producing innovative antennas/sensors. It makes use of advanced and programmable materials which show completely different behavior when subjected to external environmental conditions like hot/cold water, light, heat, etc. In contrast to the technique of 3D printing, this 4D printing is time-dependent, printer-independent, predictable, and focuses on shape/property/functionality evolution (Ref 16). The advantage of this emerging technology is that it overcomes the issues like rigidity and volume fitness which were somehow the limitations of the 3D printing technique (Ref 17-24). Thus, this technique combined with non-toxic materials such as recyclable and easily available ABS can sufficiently work as good antenna substrates to provide the advantage of flexibility, wearability, and freedom of design customization (Ref 25, 26). Using 4D printing, one can fabricate flexible and conformal resonators even much larger than the size of the printer, thus leading to the deployment of devices in tough terrains (Ref 17, 19, 24-27). It has been reported that out of various printing techniques, polyjet printing and extrusion printing are some of the most popular forms of 4D printing which support the design of tailor-made structures for bioprinting (Ref 18, 28-30).

The literature review reveals that ABS as one of the recyclable thermoplastics with excellent insulating properties is being widely used as a 3D-printed substrate for Bluetooth sensing devices. But hitherto little has been reported on the 4D capabilities of 3D-printed recyclable ABS substrate-based sensors. This study reports the rheological (melt flow), mechanical (tensile), morphological (surface hardness, roughness (Ra), porosity, etc.), 3D printability, and radio frequency (RF) characteristics of primary recycled ABS substrate. Further, the 3D-printed ABS substrate samples were exposed to two different stimuli (chemical and thermal) for 10 cycles/stages to ascertain the effect on RF characteristics for ensuring 4D capabilities. In this work, 3D-printed ABS substrates were designed and investigated that bring change in the resonator's parametrical performance. ABS has been chosen for the resonator design as it is non-biodegradable and can be easily recycled. The primary recycled ABS granules procured from the local market have been used to develop wires/feedstock filaments for 3D printing. Finally, a Bluetooth-based ring resonator/sensor has been presented which was under controlled treatments of acetone and thermal cycles to explore the 4D capabilities of the resonator.

2. Materials and Methods

To start with the material choice, initially the requirements for a resonator were explored which may be used for RF characterization. Also, this must work well with the properties like flexibility, tensile strength, brittleness, radiation characteristics, impedance bandwidth, etc. ABS opted for the reason that it has been reported as an appropriate material sufficing all the mentioned properties (Ref 11). ABS is one of the thermoplastic materials with features of 100% recyclability and abundant availability. Also, it has an excellent insulating capability which could suffice the criteria for good dielectric material (Ref 22). In this work, the effect of acetone as a stimulus on the resonator fabricated using ABS substrate has been analyzed. The resonator/sensor fabricated by using ABS as substrate material was exposed to the acetone vapors (for 10 s) and thermal cycles (the 1800s each) to study changes in the Ra and porosity of the material which could further be exploited to analyze material for its dielectric characteristics. So, the main challenge was to produce a resonator that functions satisfactorily under different environmental conditions, thus showing the time reversibility factor. Figure 1 shows the typical side view of a planar resonator/sensor.

Initially, cloth-based substrates were also explored by some researchers; however, such substrates showed deteriorated performance to typically harsh environmental conditions, thus putting restraint on the usage of such materials for dynamically changing environments. Thus, polymer-based substrates turned out to be better replacements for rigid substrates as well as cloth-based flexible substrates in terms of their shape, aperture as well as performance criteria (radiation pattern, gain, bandwidth, radiation efficiency, etc.) (Ref 28). In this work, primary recycled ABS has been used as a substrate for designing a ring resonator/sensor, typically made to work for Bluetooth applications (at 2.45 GHz). ABS being a cost-effective and readily available material emerged to be a good choice for the development of handheld products and gadgets utilizing such resonators for applications like toys, wrist bands, short-range communication devices, etc. As the utility of such devices is found in wrist bands, watches, etc., this resonator specifically used a thin Cu foil tape with good conductivity characteristics which could serve as a conductor to be placed on the substrate. Also, the same Cu foil was used to serve as a ground plane. The purpose of a good ground plane is to direct the electromagnetic waves in a required direction and help to reduce the interference, electrical noise, and detuning during its operation of transmitting or receiving. Commercially available Cu foil tape consists of a rolled Cu foil backing and an electrically conductive, pressure-sensitive acrylic adhesive. Table 1 shows the specifications of Cu foil tape used to make the structure for the ring resonator/sensor. The ring resonator structure is incomplete if the excitation is not provided to it. Therefore, edge-mounted SMA-type female right angle connectors (F R/A) were used to excite the ring resonator structure at the two ports. Table 2 specifies the characteristics of an edge-mounted SMA female (F) right angle (R/A) connector. Systematic design and analysis methodology is given in Fig. 2.
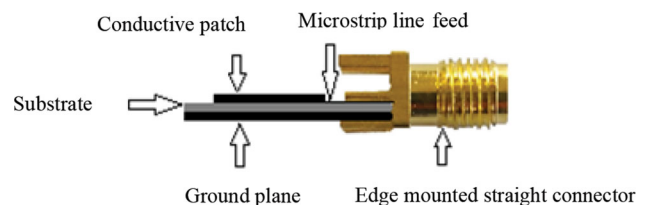
Fig. 1 Side view of a patch resonator energized through edge-mounted SubMiniature version A (SMA) female straight connector

Table 1 Specifications of Cu foil tape

Properties	Specifications
Material composition	Cu foil with pressure-sensitive conductive acrylic
Type	Foil
Foil thickness	0.04 mm
Electrical resistance	0.005 Ω
Total thickness	0.07± 0.01 mm
Adhesion strength	3.5N/10mm
Temperature range	− 40 °C to + 130 °C
Shielding effectiveness	> 75 dB, 1MHz to 2GHz

Table 2 Specifications of edge-mounted SMA F R/A connector

Properties	Specifications
Max frequency	6 GHz
Impedance	50Ω
Connector type	SMA
Orientation	Right angle
Gender	Female
Coupling mechanism	Threaded

3. Experimentation

3.1 MFI and Viscosity Analysis

Using the ASTM D1238 standard, the rheological properties of locally procured primary recycled ABS were checked (Table 3). It has been observed that the MFI data lie in the normal probability range with a standard deviation of 1.9329 for overall process capability. Process capability indices (C_p and C_{pk}) for the process were 1.472 and 1.553, respectively.

3.2 TSE

Using the Thermofisher Scientific HAAKE miniCTW twin-screw extruder, the granulated ABS were extruded at 230 °C at a load of 3.8 kg to make wire-shaped specimens that could be fed to the 3D printer. Figure 3 illustrates the filament extrusion using TSE. The printer employed in this study accepts filaments with diameters in the range of 2.5±0.05mm. These specimens of wires were then utilized to perform the mechanical and morphological analysis.

3.3 Tensile Testing

For the tensile strength analysis of extruded wire specimens, UTM (Shanta Engineering, Pune, Maharashtra, India) has been used. The mechanical properties such as peak strength, break
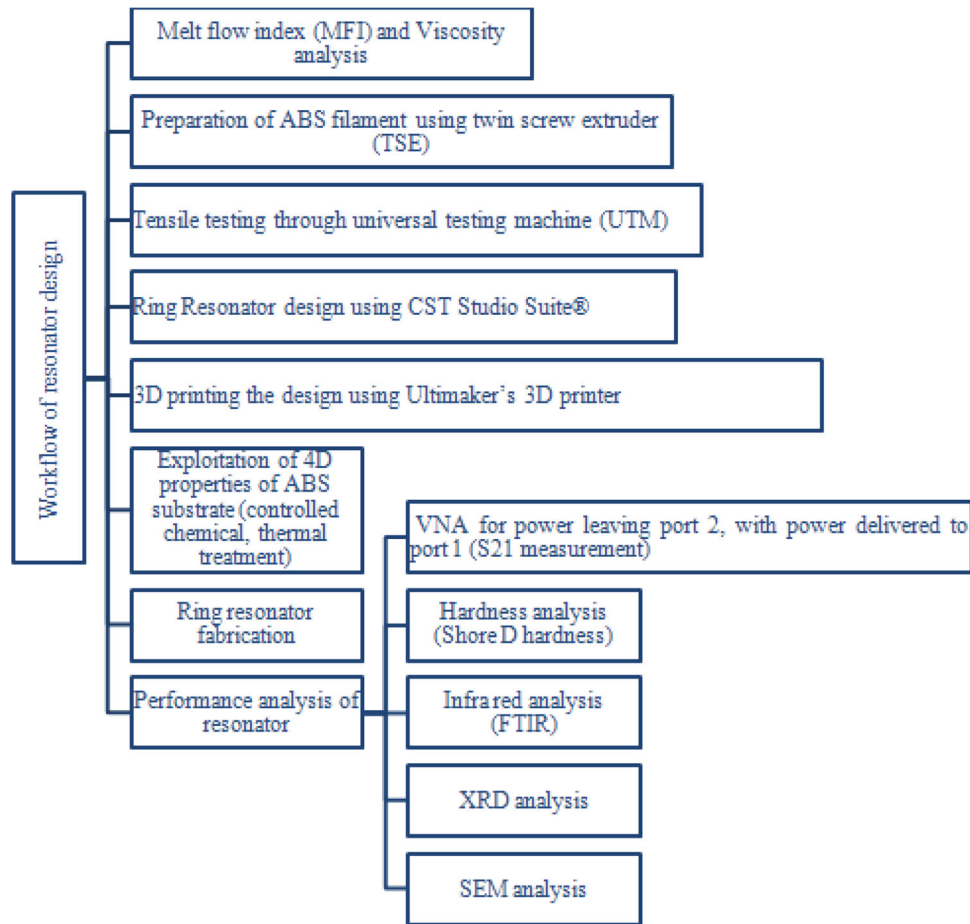
Fig. 2 Systematic design and analysis methodology

strength, Young's modulus, and modulus of toughness are shown in Table 4.

3.4 Resonator Design (Using CST Microwave Studio) and Fabrication

Before proceeding toward the actual fabrication of the ring resonator prototype on ABS substrate, the initial structure analysis has been performed on CST microwave studio suite 2019 in which the properties of ABS substrate were initially customized and then with a rigorous dimensional perusal, the radiation characteristics of the structure were examined for acceptable performance. Using the parameters shown in Table 5, for the simulative analysis, the ring resonator structure appears to be as shown in Fig. 4 (where Port 1 and Port 2 are meant to provide feed mechanism, microstrip (msl) = 1.9 mm was the microstrip width, r = 12.5 mm was the average radius calculated by using equation (1), g = 0.9 mm was the optimized gap between the ring and microstrip line and the ABS substrate was chosen to be of 40 × 50 mm). 3D printing in this study has been performed by using Ultimaker's 3D printer. The printer has a heated bed to aid an improved adhesion of ABS (primary recycled).

$$f_0 = \frac{nc}{2\pi r \sqrt{\in_{\text{eff}}}} \qquad \text{(Eq 1)}$$

Here c is the velocity of light, f is the resonant frequency, ε_{eff} is the effective dielectric constant, and n is the harmonic order of resonance.

In this study, FDM was used to 3D print substrate with the parameters as per Table 6.

3.5 A 4D Properties of ABS Substrate

Once the ε_r and tanδ (dissipation factor) were calculated, the substrate of the ring resonator was subjected to different environmental conditions which may decide its functionality as a 4D ring resonator. For the same prototype, 10 different stages/cycles have been explored according to which the resonator analysis was performed at each stage as shown in Fig. 5. Different exposure treatments include (1) exposure of the sample to acetone; (2) exposure to cold and dry temperature (0 °C) for 30 min; (3) exposure to the hot temperature of 90 °C in the oven. These stages have been decided based on ABS dissolvability in acetone and thermal treatment below the glass transition temperature of ABS. Figure 6 shows the 3D-printed prototypes exposed to various stimuli.

3.6 Resonator RF Characterization

The fabricated prototypes shown in Fig. 6 were analyzed for verifying the values of ε_r and tanδ as these parameters suffice the identity of any material meant for RF applications. Using the assumption that the common ABS material procured from the local market is having the ε_r in the range 2.7 to 3.3, the prototype was analyzed for S_{21} parameters using Rohde and Schwarz VNA. S_{21} denotes the insertion loss when the input is given to port 1 and output is analyzed at port 2 (Fig. 7).

By putting the values of parameters in the set of equations (Ref 8), the value of the ε_r of the material was calculated. Using Equations (2-5), the value of ε_r of the material is 2.4 and tanδ is 0.0045. The relative ε_r was calculated by putting resonant frequency observed from VNA, f_0 = 2.68 GHz, average radius of the ring, r_m =12.5 mm, the height of substrate, h=0.75 mm, width of the strip, w=1.9 mm and thickness of trace, t=0.08 mm

$$\in_r = \frac{2 \in_{\text{eff}} + M - 1}{M + 1} \qquad \text{(Eq 2)}$$

$$\in_{\text{eff}} = \left(\frac{nc}{2\pi r_m f_0} \right)^2 \qquad \text{(Eq 3)}$$

$$M = \left(1 + \frac{12h}{w_{\text{eff}}} \right)^{-0.5} \qquad \text{(Eq 4)}$$

$$w_{\text{eff}} = w + \frac{1.25t}{\pi} \left[1 + \ln \left(\frac{2h}{t} \right) \right] \qquad \text{(Eq 5)}$$

The tanδ of the substrate was calculated by using Eq 6.

$$\tan \delta = \frac{\alpha_d \lambda_0 \sqrt{\in_{\text{eff}}} (\in_r - 1)}{8.686\pi \varepsilon_r (\in_{\text{eff}} - 1)} \qquad \text{(Eq 6)}$$

where α_d can be calculated with the help of α_{total} by using Eqs 7, 9, and 10

$$\alpha_{total} = \alpha_c + \alpha_d + \alpha_r \qquad \text{(Eq 7)}$$

Table 3   MFI and viscosity values for ABS sample

S.No.	MFI in g/, 10min	Density in g/ cm³	Viscosity in Pa-s
1.	11	1.096×10^{-3}	70931.2
2.	12.33	1.455×10^{-3}	76351.4
3.	15.2	1.456×10^{-3}	61572.3
4.	11.4	1.666×10^{-3}	42010.4
5.	10.2	1.513×10^{-3}	70547.5

(a)   (b)

Fig. 3 (a) Extrusion of ABS filament and (b) extruded filament

Table 4 Observed mechanical properties

Sample No.	Peak load, kN	Peak elongation, mm	Break load, kN	Break elongation, mm	Peak strength, kN/Sq.mm	Break strength, kN/Sq.mm	% Peak elongation	% Break elongation	Peak strain	Break strain	Modulus of toughness, Pa	Young's modulus, MPa
1	141.7	2.1	127.53	2.31	28.88	25.99	4	5	0.042	0.0462	0.600369	687.619
2	76.9	4.62	69.21	5.04	15.67	14.11	9	10	0.0924	0.1008	0.711144	169.5887
3	97	2.31	87.3	2.73	19.77	17.79	5	5	0.0462	0.0546	0.485667	427.9221

Attenuation constant in the conductor α_c can be calculated using equation in (8)

For $\dfrac{w}{h} \leq \dfrac{1}{2\pi}$ (Eq 8)

$$\alpha_c = \frac{8.68 R_s}{2\pi Z_0 h}\left[1 - \left(\frac{w_{\text{eff}}}{4h}\right)^2\right]\left\{1 + \frac{h}{w_{\text{eff}}} + \frac{h}{\pi w_{\text{eff}}}\left[\ln\left(\frac{4\pi w}{t} + 1\right) - \frac{1 - \frac{t}{w}}{1 + \frac{t}{4\pi w}}\right]\right\} dB/\text{unit length}$$

For $\dfrac{1}{2\pi} < \dfrac{w}{h} < 2$

$$\alpha_c = \frac{8.68 R_s}{2\pi Z_0 h}\left[1 - \left(\frac{w_{\text{eff}}}{4h}\right)^2\right]\left\{1 + \frac{h}{w_{\text{eff}}} + \frac{h}{\pi w_{\text{eff}}}\left[\ln\left(\frac{2h}{t} + 1\right) - \frac{1 - \frac{t}{h}}{1 + \frac{t}{2h}}\right]\right\} dB/\text{unit length}$$

For $\dfrac{w}{h} > 2$

$$\alpha_c = \frac{R_s}{Z_0 h}\frac{8.68}{\left\{\frac{w_{\text{eff}}}{h} + \frac{2}{\pi}\ln\left[2\pi e\left(\frac{w_{\text{eff}}}{2h} + 0.94\right)\right]\right\}^2}\left[\frac{w_{\text{eff}}}{h} + \frac{\frac{w_{\text{eff}}}{\pi h}}{\frac{w_{\text{eff}}}{2h} + 0.94}\right]$$

$$\left\{1 + \frac{h}{w_{\text{eff}}} + \frac{h}{\pi w_{\text{eff}}}\left[\ln\left(\frac{2h}{t} + 1\right) - \frac{1 - \frac{t}{h}}{1 + \frac{t}{2h}}\right]\right\} dB/\text{unit length}$$

$$R_s = \sqrt{\frac{\pi \mu_0 f_0}{\sigma_{Cu}}}\left\{1 + \frac{2}{\pi}\tan^{-1}\left[1.4\left(\frac{\Delta}{\delta_s}\right)^2\right]\right\}$$

$$\text{where } \delta_s = \sqrt{\frac{1}{\pi \sigma \mu_0 f_0}}$$

Radiation loss attenuation constant α_r can be calculated using equations in (9)

$$\alpha_r = \frac{\pi}{Q_r \lambda_g} Np/\text{unit length} \tag{Eq 9}$$

$$\text{where, } Q_r = \frac{\in_{\text{eff}} Z_0}{120\pi^3 \left(h/\lambda_0\right)^2 \left(1 - \frac{4}{3}\varepsilon_r + \frac{8}{15}f_r^2\right)}$$

Total loss in attenuation can be calculated by using equations in (10)

$$\alpha_{\text{total}} = \frac{\pi}{Q_0 \lambda_g} Np/\text{unit length} \tag{Eq 10}$$

$$\text{where } Q_0 = \frac{Q_L}{1 - 10^{-L_A/20}}$$

$$Q_L = \frac{f_0}{BW_{-3dB}}$$

4. Results and Discussion

4.1 4D Characterization

The optical-based images of the prototypes have been captured by using SEM at ×100 magnification. The percentage of porosity of the chemically treated prototypes was recorded

using QSMIAS 4.0 image analysis tool as per ASTM B 276 standard. Table 7 specifies in detail the stage-wise surface textural properties in terms of the zones of porosity, porosity percentage, 3D rendered image, and average Ra of the prototypes. In comparison with stage 1, it is observed that the porosity decreases at stage 3 with a simultaneous decrease in average Ra of the substrate prototype which is but obvious due to the reflow of ABS material from peaks to valleys. However, another similar treatment at stage 6 results in an increase in Ra and porosity (although less than the parent value), most likely due to the increase of air voids at that stage. On the further repetition of similar treatment, the porosity again decreased with a drastic improvement in Ra indicating the 4D characteristic of the existing ABS.

4.2 Hardness Testing

The hardness analysis of the prototypes (of stages 1, 3, 6, and 9 as per Fig. 6) was performed by the Shore D hardness tester (range 0-100) as per ASTM D 2240. For the repeatability, the hardness was observed at three different locations of the prototype and hence the average value of hardness was recorded as given in Table 8. It should be noted that there is

a maximum of 5% change in the value of hardness showing that such materials can serve as substrates for the conformal application of resonating structures under selected environmental conditions. Further based upon Table 7, the surface characteristics (amplitude distribution function, bearing ratio curve, and peak count) of substrates at stages 1, 3, 6, and 9 were plotted which are in close confirmation with Ra profiles.

4.3 FTIR Analysis

The attenuated total reflection (ATR) equipped Fourier transformed infrared (FTIR) spectroscopic analysis of samples 1, 3, 6, and 9 was performed to investigate the changes that occurred in the chemical structure of ABS substrate due to the chemical/thermal treatment as a stimulus. Figure 8 shows the absorbance spectrum for ABS samples as per Fig. 6. The range of wavenumber (WN) for the analysis of the test was from 4000 to 400 cm^{-1}. The significant shifts were observed in ABS absorbance peaks that outlined the changes in its chemical structure by chemical treatment. For a 3200-3000 cm^{-1} range of WN, absorbance peaks were observed that highlight the

Table 5 Parametric values for the structure

Parameter	Value
Frequency of operation, f	2.45 GHz
Dielectric constant, ε_r	3
Loss tangent, $\tan\delta$	0.006
Height of the substrate, h	0.75 mm
Thickness of the trace, t	0.08 mm

Table 6 Input process parameters for 3D printing

Parameters	Values
Infill density	100%
Infill pattern	Rectilinear
Layer height	0.25mm
Nozzle temperature	250 °C
Bed temperature	60 °C
Raster angle	45°

(a)

(b)
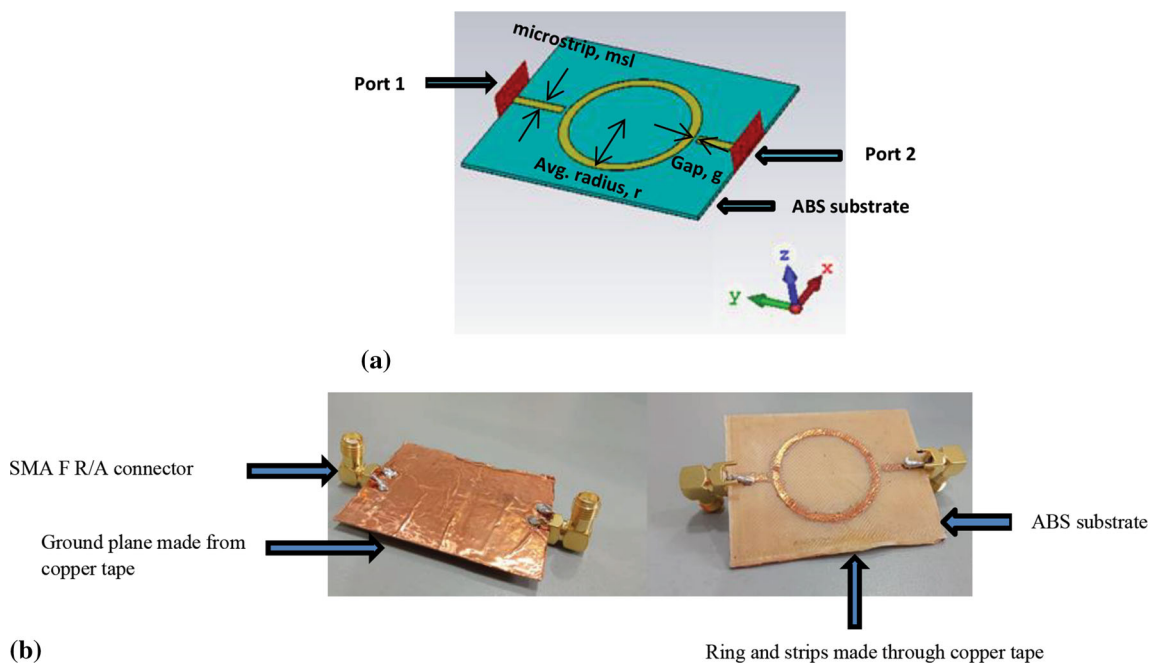
Fig. 4 Ring resonator structure design (a) in CST microwave studio 2019 and (b) Bird's eye view of the fabricated prototype
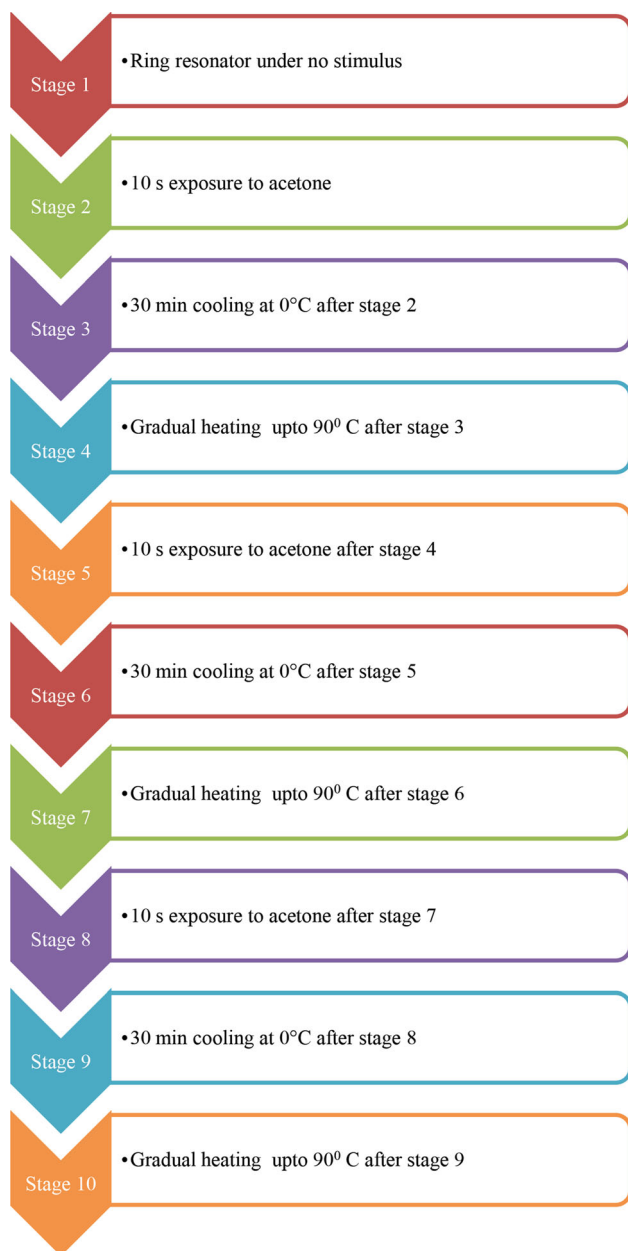
Fig. 5 Stage-wise description of the exposure treatments given to ring resonator prototype

presence of the C-H functional group. The chemical treatment on substrate significantly increased the absorbance peaks up to stage 9 (shown in sample 9) as symmetrical stretching vibrations were observed in sample 9 (Fig. 9) for the 3200-3000cm^{-1} WN range. It was observed that no clear or strong peaks were observed in the same WN range for the C-H group in the case of sample 3 and sample 6. The presence of the C ≡ N functional group in sample 1 was observed for IR range 1375-1500cm^{-1} WN with weak intensity peaks. The hardening of C ≡ N functional group chemical bonds was observed due to shifting and stretching of its peaks from the actual range toward the left side IR range 2000-2250cm^{-1} WN. For sample 3 and

sample 6, the observations vibration peaks (in the 2000-2250cm^{-1} WN range) show the acceptable effect of chemical treatment on Shore D hardness properties of ABS. The same peaks as of sample 1 were obtained finally again in sample 9, and strong absorbance peaks at 1375-1500cm^{-1} WN range were recorded. Also, strong absorbance peaks for C=C were observed at 1638-1665cm^{-1} WN for sample 9 (stage 3 chemical treatment). This increase in absorbance of ABS after treatment shows the programmability properties in it. The FTIR analysis shows that the chemical structure of ABS may be programmed to increase/decrease the mechanical, morphological properties, and hardness in such a manner that the programmed 3D-printed substrate shows 4D properties.

4.4 XRD Analysis

The changes that occurred in the crystal structure of ABS after chemical treatment was investigated by XRD analysis. XRD testing of ABS substrate samples 1, 3, 6, and 9 was performed, and diffraction patterns were collected. Figure 9 shows the XRD diffraction pattern of 3D-printed ABS substrate collected at a range of angle 2θ between 10 and 100.397° keeping the scanning rate 5°/min.

The XRD spectrum was plotted for intensity v/s 2θ for each sample. The comparison of samples 1 and 3 and XRD signature analysis outlined that chemical treatment significantly changed the crystal structure of the 3D-printed ABS prototype after first stage of exposure. The peak shift was observed for sample 1 at two specific values of 2θ, i.e., 64.481° and 77.682°, respectively. The same peaks for sample 3 were obtained with a shift at 64.572° and 77.826° that resulted in increased Shore D hardness of ABS after the chemical reaction. The maximum shift of 0.12° in the first peak was finally observed (in sample 9) as compared to the peak of sample 1. Also, a maximum of 0.144° peak shift was observed in the second peak after the chemical treatment of ABS. The XRD analysis supports the outcomes of FTIR analysis that the solvent significantly changes the chemical properties and crystal structure of the ABS polymer matrix as a result of which the desired properties of the matrix may be programmed and customized by changing the bond strength and bond angles for 4D applications.

4.5 RF Characterization

Initially, the simulated and experimental designs were compared to calculate the exact ε_r and tanδ of the material. The ε_r dictates the charge holding capacity of material and tanδ, also known as dissipation factor, accounts for the loss of RF signal in the material itself. Figure 10 shows that the first resonance occurs at around 2.45GHz as the resonator is designed for so, but the experimental first resonance is seen at 2.68 GHz. This is because the calculation process (Eq 1) started with an assumption that the dielectric constant of ABS is 3 (usually it varies in the range 2.4-3.6). However, through the set of Eq 2-10 and VNA analysis, it was found out to be 2.4 GHz, thus resulting in a right frequency shift.

Comparison of Stages 1, 3, 6, and 9 is of significant interest as they decide the change in behavior of the substrate material and its RF characteristics (Frequency shift, dielectric behavior). This is because at these stages the controlled exposure to
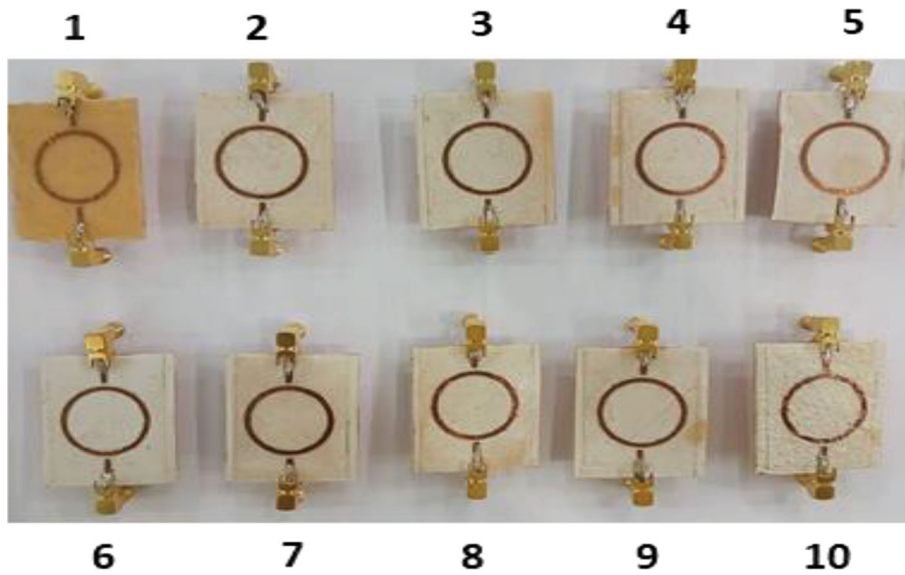
Fig. 6 Stage-wise ABS ring resonator prototypes
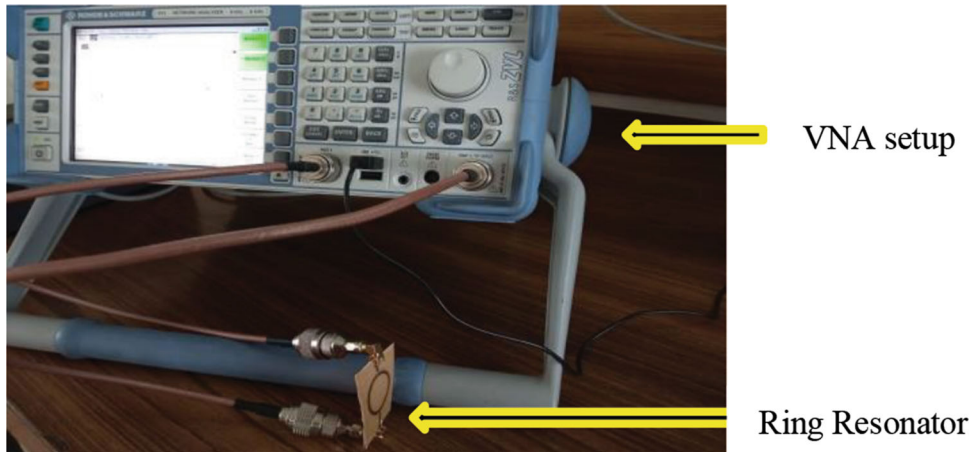
Fig. 7 VNA testing of the fabricated prototype

acetone has changed the material's peak and valley formations. Figure 11 and Table 9 depict the resonant frequency shift and the change in values of the S_{21} magnitude due to the controlled stimuli. It is observed that there is a gradual increase in ε_r of the material with a minimal increase in the value of dissipation loss in the material. Also, the little shifts in resonant frequency correspond to the unintentional porosity incurred during the FDM process. Also, higher ε_r means a higher dielectric strength and hence good insulating properties as a resonator substrate, thus leading to a conclusion that the fourth dimension of chemical treatment added to 3D-printed substrate can result in a category of tailored substrates which may achieve better insulating properties and more miniaturization (antenna size and ε_r have an inverse relationship) to fit into a compact world.

5. Conclusions

The following are conclusions from this study:

(1) With a motivation to bring a value-added product from a non-biodegradable material, Bluetooth sensor has been successfully prepared for 2.45GHz.

Table 7   Morphological analysis of the prototypes in terms of different parameters
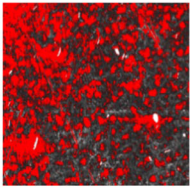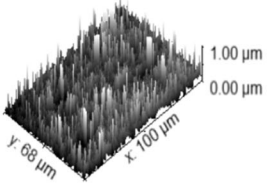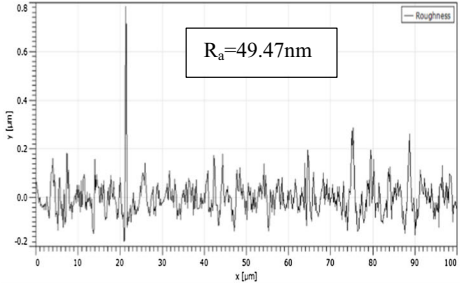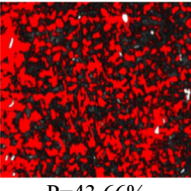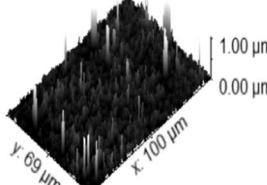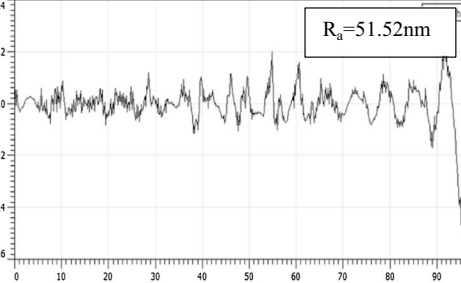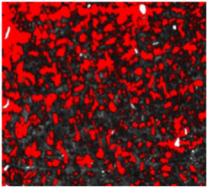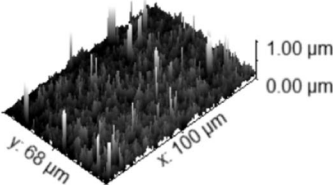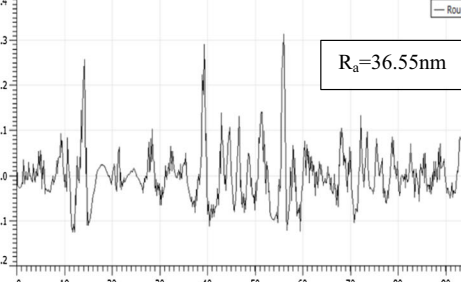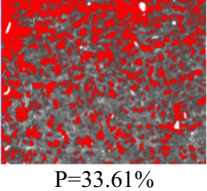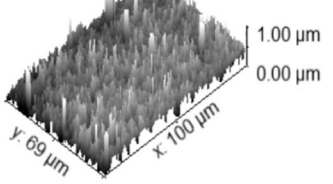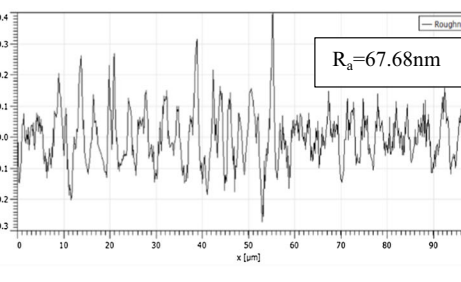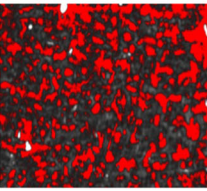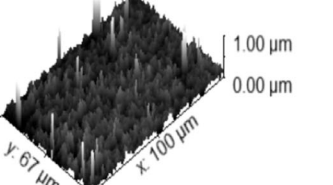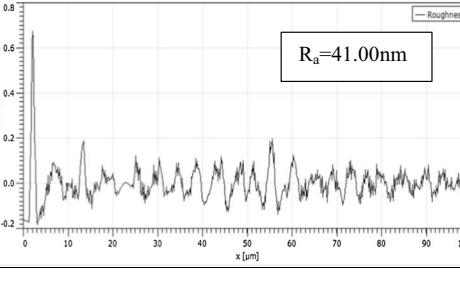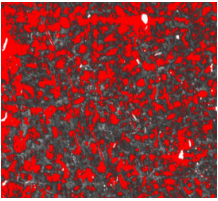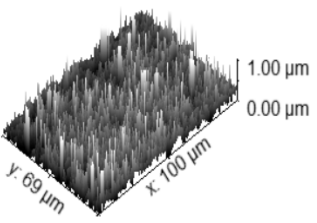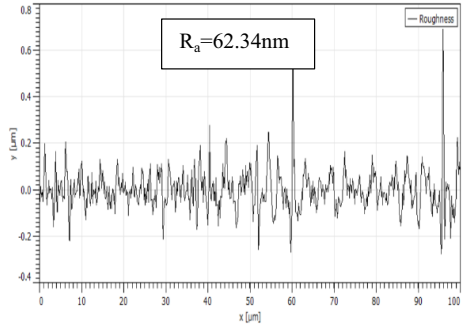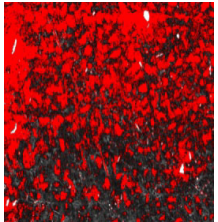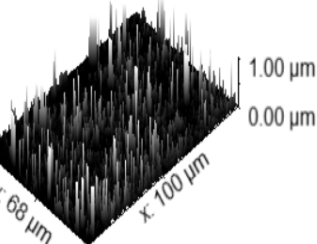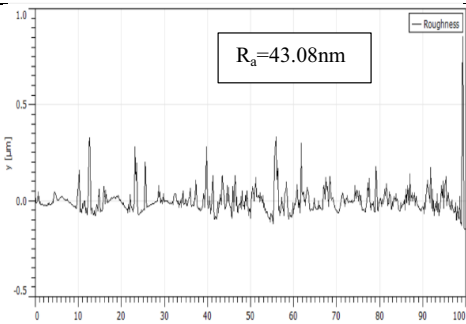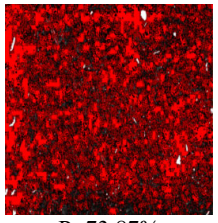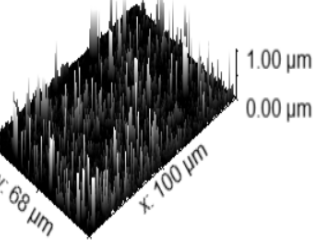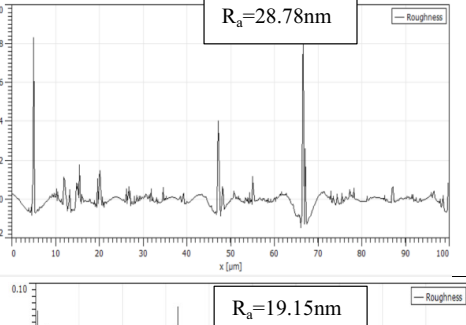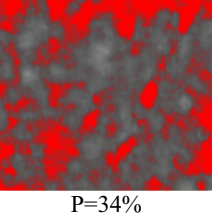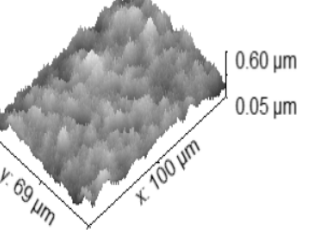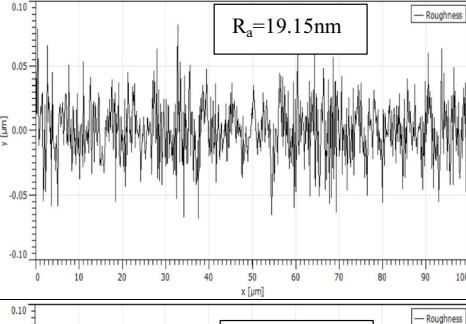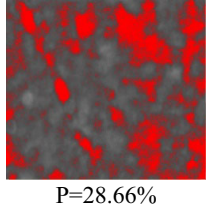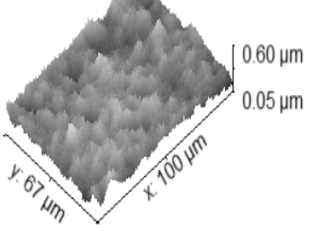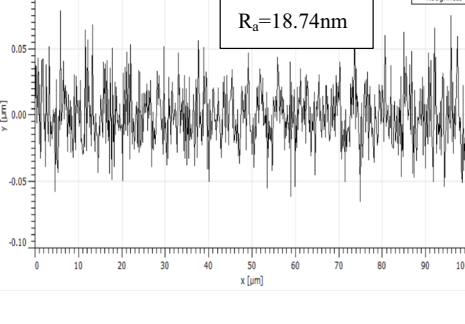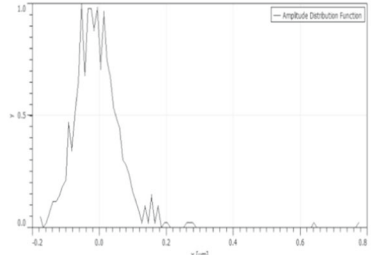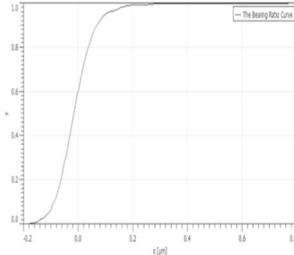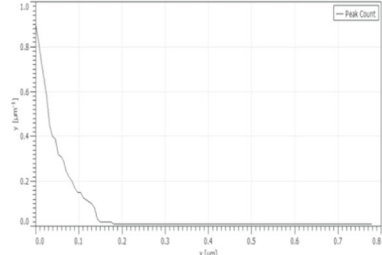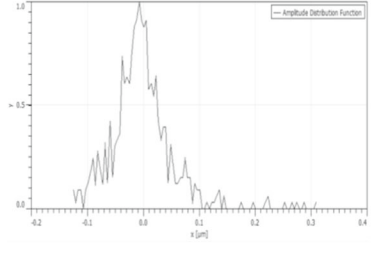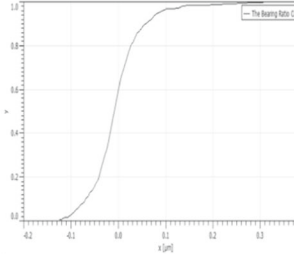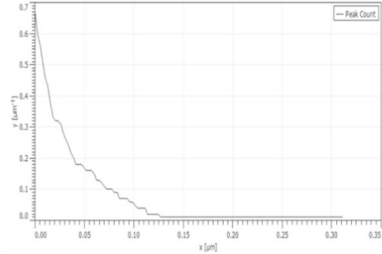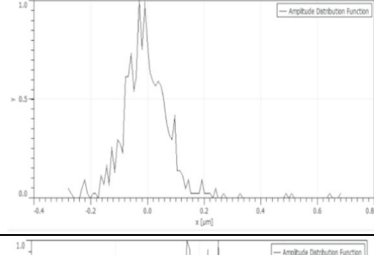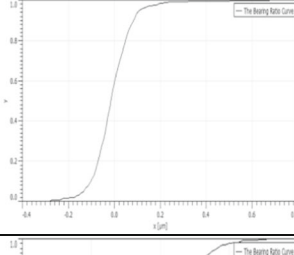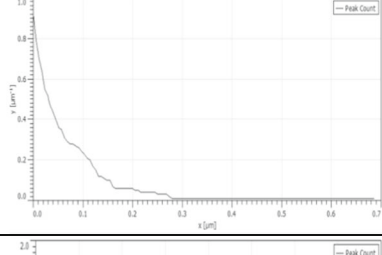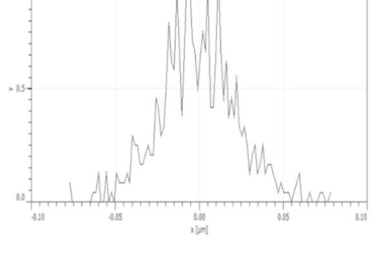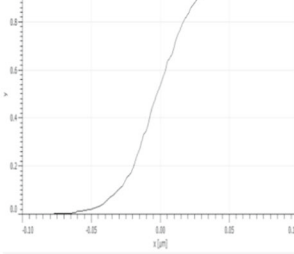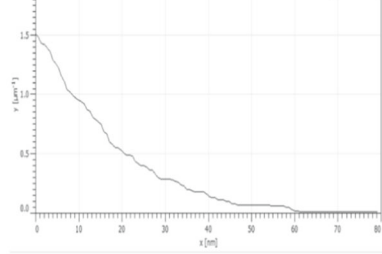
Stage	Parameters		
	Porosity (%)	3D rendered Image	Roughness (R_a)
Stage 1	 P=39.77%		 R_a=49.47nm
Stage 2	 P=43.66%		 R_a=51.52nm
Stage 3	 P=34.3%		 R_a=36.55nm
Stage 4	 P=33.61%		 R_a=67.68nm
Stage 5	 P=32.68%		 R_a=41.00nm

Table 7   continued

Stage	Porosity (%)	3D rendered Image	Roughness (R)
		Parameters	
Stage 6	P=37.73%	1.00 µm / 0.00 µm, y: 69 µm, x: 100 µm	R_a=62.34nm
Stage 7	P=55.75%	1.00 µm / 0.00 µm, y: 68 µm, x: 100 µm	R_a=43.08nm
Stage 8	P=73.87%	1.00 µm / 0.00 µm, y: 68 µm, x: 100 µm	R_a=28.78nm
Stage 9	P=34%	0.60 µm / 0.05 µm, y: 69 µm, x: 100 µm	R_a=19.15nm
Stage 10	P=28.66%	0.60 µm / 0.05 µm, y: 67 µm, x: 100 µm	R_a=18.74nm

Table 8 Material properties in terms of its hardness, ADF, BRC, and peak count

Stages	Parameters			
	Hardness using Shore-D Durometer	Amplitude Distribution Function	Bearing Ratio Curve	Peak Count
1	50			
3	52.5			
6	52.5			
9	51			

(2) The substrate material was exposed to controlled chemical/ thermal treatments to exploit its 4D behavior. When used as an insulating material for fabricating resonator substrates, it effectively displays 4D printing properties as it extensively shows a change in porosity and average Ra value with almost reaching back to the parent value in the final treatment for different stages of controlled chemical and heat treatments. The percentage variation in the dielectric constant has been recorded to a maximum of 8% (in stage 9) and a minimum of 2% (in stage 6). Also, the dissipation factor of the substrate has been recorded to remain constant ($\sim$0.0045) indicating a factor of repeatability and hence the usability of such materials for 4D printing applications.

(3) The surface features such as hardness, Ra profile have shown a close relationship with amplitude distribution function, bearing ratio curve, and peak count to affect the RF characteristics in different stages of processing. These results have been well supported with FTIR and XRD analyses.

(4) The detailed RF characterization of all 4D-printed prototypes shows that a controlled subjection to chemical and temperature conditions results in a category of tailored substrates with miniaturized antenna designs. The value for ε_r decides the capacity of a sample to hold the charge. Thus, an almost same value of ε_r with a low value of dissipation factor plays a vital role in improving the characteristics of the resonator and supporting the
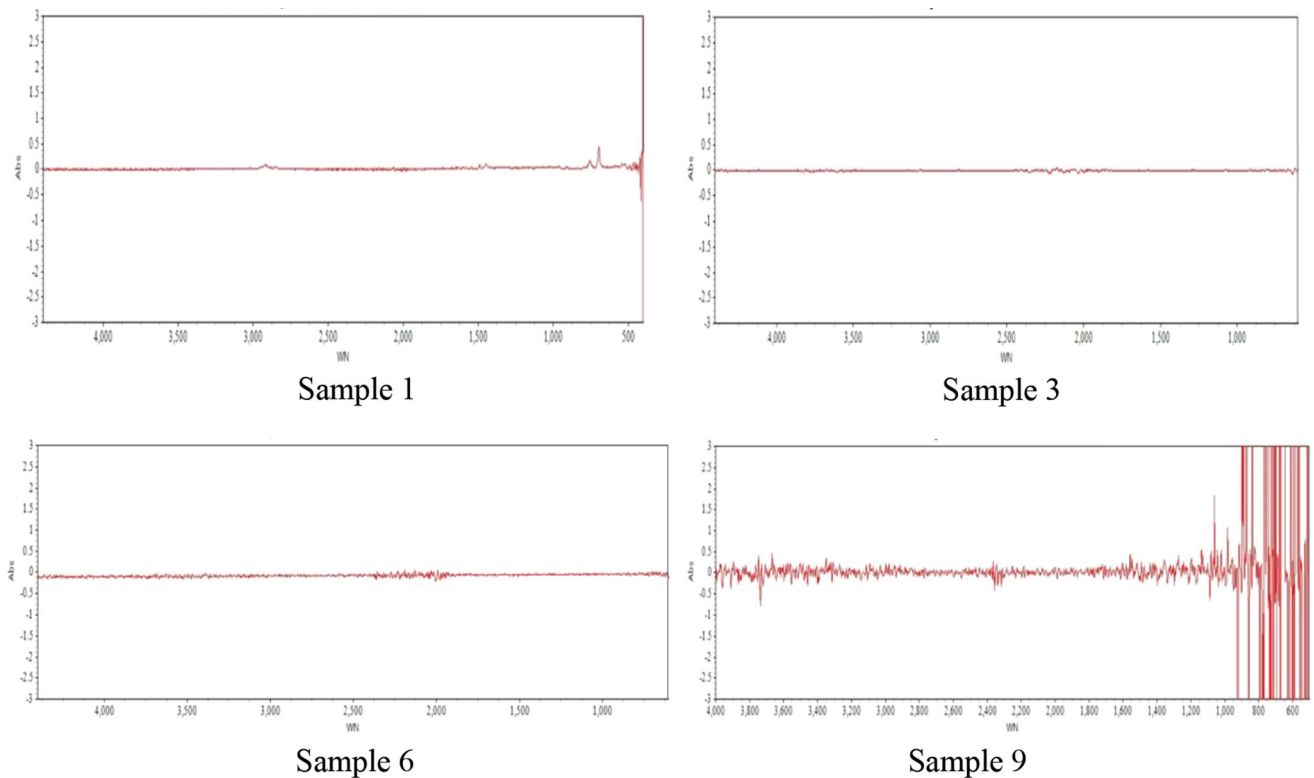
Fig. 8 FTIR analysis at different stages of controlled exposure as per Fig. 6
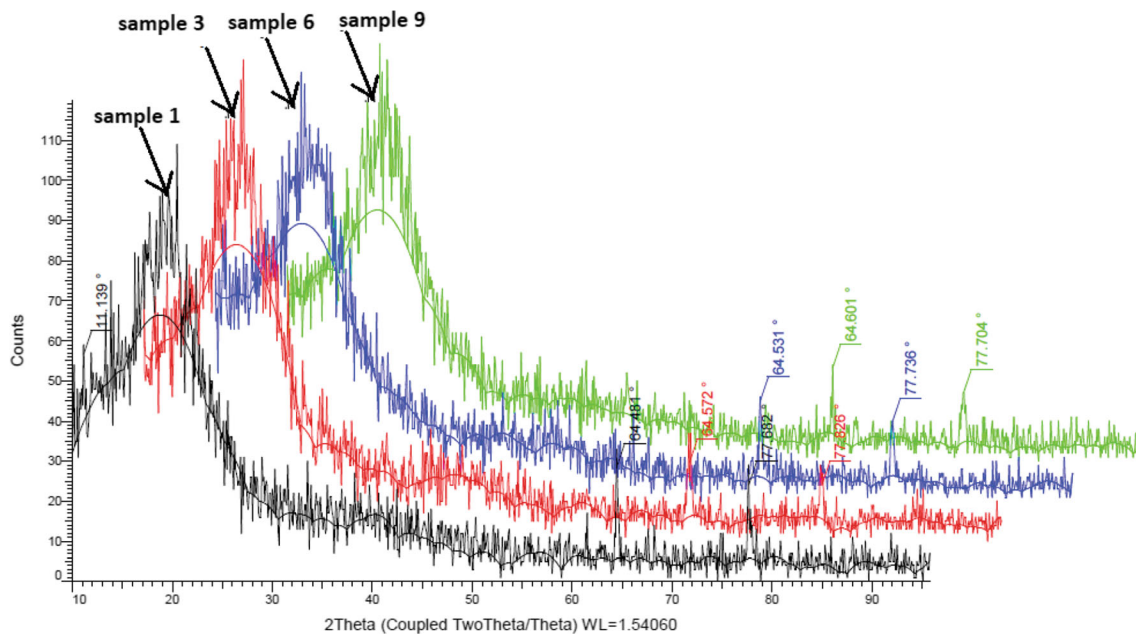
Fig. 9 XRD analysis of the ring resonator prototypes at different stages of stimuli as per Fig. 6

repeatability in the response required for 4D printing. This may lead to the design of resonators which can be typically mounted in difficult climatic terrains without any compromise in their radiation performance.

Further investigations may include the experimentations related to the 4D analysis of other non-biodegradable reinforcements in ABS or other thermoplastic/thermosetting polymers for better waste management. Also, such substrates may further be investigated for different types of sensor/antenna applications showing multiband behavior functionality apart from Bluetooth utility. In this study, the 3D printing of ABS substrate was performed at fixed settings and the design of the experiment was not followed for optimizing the FDM printed part properties (in terms of mechanical, surface, morphological
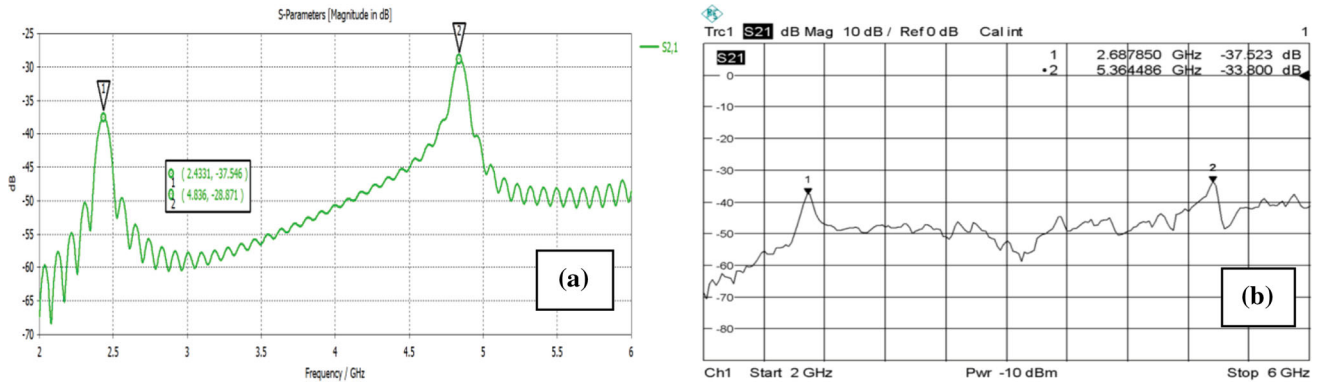
Fig. 10 Insertion loss (S_{21}) values of the prototype Stage 1: (a) simulated and (b) experimental
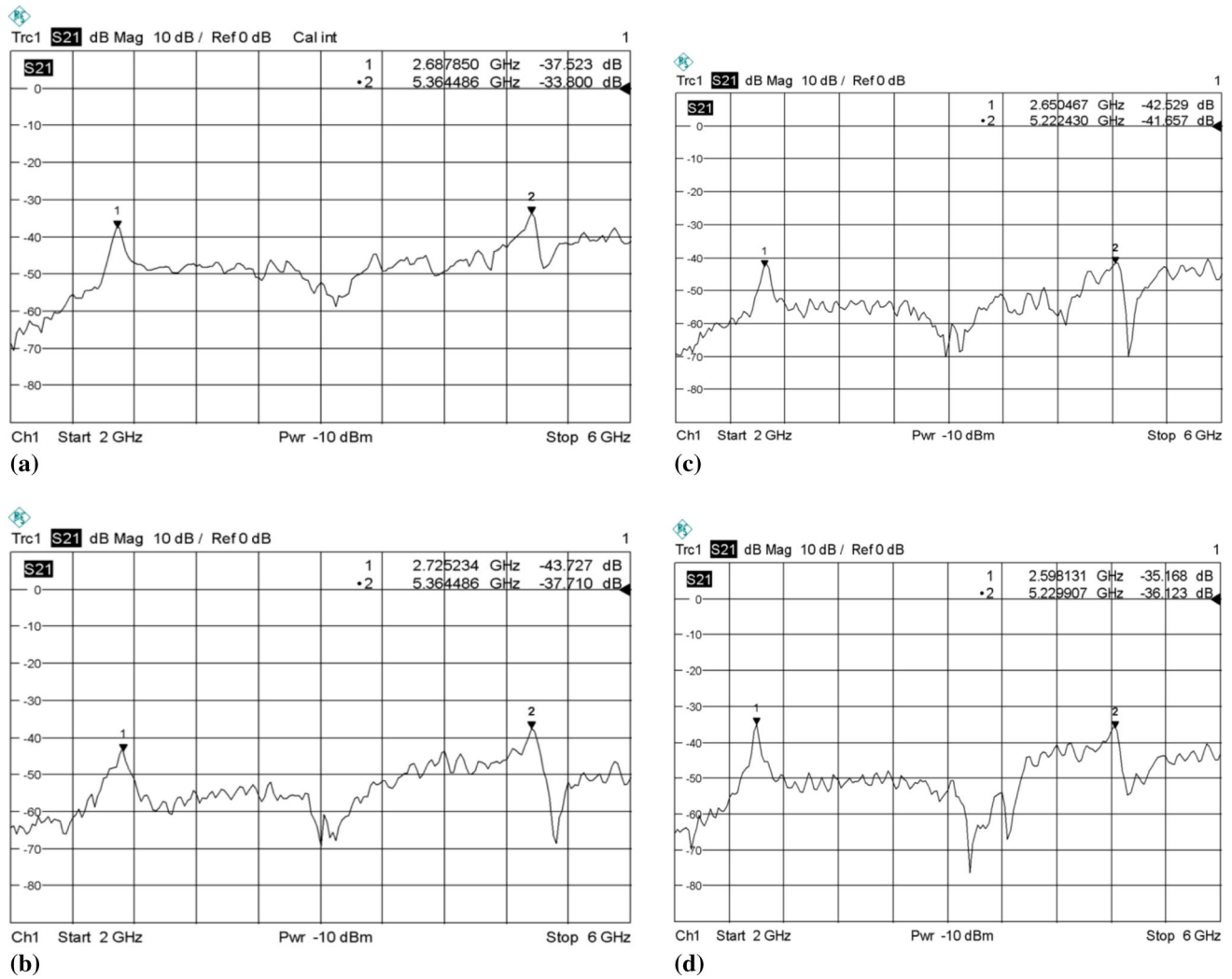
Fig. 11 Description of frequency shift and S_{21} magnitude change: (a) stage 1; (b) stage 3; (c) stage 6; (d) stage 9

Table 9 Stage-wise illustration of RF characteristics of chemically/thermally treated prototypes

Stages	Parameters			
	Dielectric constant, ε_r	Loss tangent, tan δ	1st resonance, in GHz	S_{21} at first resonance, in dB
Stage 1	2.44	~0.0045	2.68	− 37.52
Stage 2	2.54	~0.0045	2.63	− 45.00
Stage 3	2.35	~0.0045	2.72	− 43.72
Stage 4	2.49	~0.0045	2.65	− 41.30
Stage 5	2.49	~0.0045	2.65	− 42.66
Stage 6	2.49	~0.0045	2.65	− 42.52
Stage 7	2.54	~0.0045	2.62	− 58.84
Stage 8	2.06	~0.0053	2.87	− 30.08
Stage 9	2.64	~0.0045	2.59	− 35.16
Stage 10	1.53	~0.0038	3.25	− 27.44

features), but for establishing the 4D capabilities with FDM these parameters may be considered in future applications.

References

1. D.C. Thompson, O. Tantot, H. Jallageas, G.E. Ponchak, M.M. Tentzeris, and J. Papapolymerou, Characterization of Liquid Crystal Polymer (LCP) Material and Transmission Lines on LCP Substrates from 30 to 110 GHz, *IEEE Trans. Microw. Theory Tech.*, 2004, **52**(4), p 1343–1352.

2. D.A. Rudy, J.P. Mendelsohn, and P.J. Muniz, Measurement of RF Dielectric Properties with Series Resonant Microstrip Elements, *Microw. J.*, 1998, **41**(3), p 22–32.

3. C.C. Njoku, W.G. Whittow, and J.C. Vardaxoglou, Effective Permittivity of Heterogeneous Substrates with Cubes in a 3-D Lattice, *IEEE Antennas Wirel. Propag. Lett.*, 2011, **10**, p 1480–1483.

4. B.S. Cook, and A. Shamim, Inkjet Printing of Novel Wideband and High Gain Antennas on Low-Cost Paper Substrate, *IEEE Trans. Antennas Propag.*, 2012, **60**(9), p 4148–4156.

5. H.F. Abutarboush, and A. Shamim, Paper Based Inkjet-Printed Tri-Band U-Slot Monopole Antenna for Wireless Applications, *IEEE Antennas Wirel. Propag. Lett.*, 2012, **11**, p 1234–1237.

6. Y. Al-Naiemy, T.A. Elwi, H.R. Khaleel, and H. Al-Rizzo, A Systematic Approach for the Design, Fabrication, and Testing of Microstrip Antennas Using Inkjet Printing Technology, *Int. Sch. Res. Not.*, 2012, **2012**, p 1–11.

7. S. Zhang, C.C. Njoku, W.G. Whittow, and J.C. Vardaxoglou, Novel 3D Printed Synthetic Dielectric Substrates, *Microw. Opt. Technol. Lett.*, 2015, **57**(10), p 2344–2346.

8. M. Mirzaee, S. Noghanian, L. Wiest, I. Chang, Developing flexible 3D Printed Antenna Using Conductive ABS materials. In *2015 IEEE International Symposium on Antennas and Propagation & USNC/URSI National Radio Science Meeting*. (IEEE, 2015). pp. 1308-1309

9. M. Mirzaee, *Developing Novel 3D Antennas Using Advanced Additive Manufacturing Technology*. The University of North Dakota (2015)

10. A.M. Mansour, N. Shehata, B.M. Hamza, and M.R.M. Rizk, Efficient Design of Flexible and Low Cost Paper-Based Inkjet-Printed Antenna, *Int. J. Antennas Propag.*, 2015, **2015**, p 1–6.

11. S. Ahmed, F.A. Tahir, A. Shamim, and H.M. Cheema, A Compact Kapton-Based Inkjet-Printed Multiband Antenna for Flexible Wireless Devices, *IEEE Antennas Wirel. Propag. Lett.*, 2015, **14**, p 1802–1805.

12. S. Moscato, R. Bahr, T. Le, M. Pasian, M. Bozzi, L. Perregrini, and M.M. Tentzeris, Infill-Dependent 3-D-Printed Material Based on NinjaFlex Filament for Antenna Applications, *IEEE Antennas Wirel. Propag. Lett.*, 2016, **15**, p 1506–1509.

13. H. D. Nguyen, J. P. Coupez, V. Castel, C. Person, A. Delattre, L. Crowther-Alwyn, and P. Borel, RF Characterization of Flexible Substrates for New Conformable Antenna Systems. In *2016 10th European Conference on Antennas and Propagation (EuCAP)* (pp. 1-5). IEEE (2016)

14. M. Mirzaee, and S. Noghanian, Additive manufacturing of a compact 3D Dipole Antenna Using ABS Thermoplastic and High Temperature Carbon Paste. In *2016 IEEE International Symposium on Antennas and Propagation (APSURSI)* (pp. 475-476). IEEE (2016)

15. M. Ramadan, and R. Dahle, Characterization of 3-D Printed Flexible Heterogeneous Substrate Designs for Wearable Antennas, *IEEE Trans. Antennas Propag.*, 2019, **67**(5), p 2896–2903.

16. G. Zou, H. Gronqvist, J.P. Starski, and J. Liu, Characterization of Liquid Crystal Polymer for High Frequency System-in-a-Package Applications, *IEEE Trans. Adv. Packag.*, 2002, **25**(4), p 503–508.

17. R. Sharma, R. Singh, and A. Batish, On Effect of Chemical-Assisted Mechanical Blending of Barium Titanate and Graphene in PVDF for 3D Printing Applications. J. Thermoplast Compos. Mater. 0892705720945377 (2020)

18. S. Singh, S. Ramakrishna, and R. Singh, Material Issues in Additive Manufacturing: A Review, *J. Manuf. Process.*, 2017, **25**, p 185–200.

19. F. Momeni, X. Liu, and J. Ni, A Review of 4D Printing, *Mater. Des.*, 2017, **122**, p 42–79.

20. J.S. Chohan, and R. Singh, Pre and Post Processing Techniques to Improve Surface Characteristics of FDM Parts: A State of Art Review and Future Applications, *Rapid Prototyp. J.*, 2017, **23**(1), p 495–513.

21. X. Kuang, D.J. Roach, J. Wu, C.M. Hamel, Z. Ding, T. Wang, and H.J. Qi, Advances in 4D Printing: Materials and Applications, *Adv. Func. Mater.*, 2019, **29**(2), p 1805290.

22. W. Clower, M.J. Hartmann, J.B. Joffrion, and C.G. Wilson, Additive Manufactured Graphene Composite Sierpinski Gasket Tetrahedral Antenna for Wideband Multi-Frequency Applications, *Addit. Manuf.*, 2020, **32**, p 101024.

23. M. Dahim, M. Abuaddous, R. Ismail, H. Al-Mattarneh, and A. Jaradat, Using a Dielectric Capacitance Cell to Determine the Dielectric Properties of Pure Sand Artificially Contaminated with Pb, Cd, Fe, and Zn. Appl. Environ. Soil Sci. 2020 (2020)

24. V. Kumar, R. Singh, and I. P. S. Ahuja, Secondary Recycled Acrylonitrile–Butadiene–Styrene and Graphene Composite for 3D/4D Applications: Rheological, Thermal, Magnetometric, and Mechanical Analyses. J. Thermoplast. Compos. Mater. 0892705720925114. (2020)

25. I. L. Costa, P. H. Pereira, A. M. Claro, N. C. D. Amaral, H. D. S. Barud, R. B. Ribeiro, and D. R. Mulinari, 3D-Printing Pen from Valorization of Pine Cone Residues as Reinforcement in Acrylonitrile Butadiene Styrene (ABS): Microstructure and Thermal Properties. J. Thermoplast. Compos. Mater. 08927057211012735 (2021)

26. A.K. Cress, J. Huynh, E.H. Anderson, R. O'neill, Y. Schneider, and Ö. Keleş, Effect of Recycling on the Mechanical Behavior and Structure of Additively Manufactured Acrylonitrile Butadiene Styrene (ABS), *J. Clean. Product.*, 2021, **279**, p 123689.

27. L. Wu, J. Huang, M. Zhai, B. Sun, H. Chang, S. Huang, and H. Liu, Deformable Bowtie Antenna Realized by 4D Printing, *Electronics*, 2021, **10**(15), p 1792.

28. C. Jain, B.S. Dhaliwal, and R. Singh, Flexible and Wearable Patch Antennas Using Additive Manufacturing: A Framework, *Ref Mod. Mater. Sci. Mater. Eng.*, 2021 https://doi.org/10.1016/B978-0-12-820 352-1.00093-6

29. E. MacDonald, D. Espalin, D. Doyle, J. Muñoz, S. Ambriz, J. Coronel, and R. Wicker, Fabricating Patch Antennas within Complex Dielectric Structures Through Multi-Process 3D Printing, *J. Manuf. Process.*, 2018, **34**, p 197–203.

30. M. Barletta, A. Gisario, and M. Mehrpouya, 4D Printing of Shape Memory Polylactic Acid (PLA) Components: Investigating the Role of the Operational Parameters in Fused Deposition Modelling (FDM), *J. Manuf. Process.*, 2021, **61**, p 473–480.